Chemical Engineering Journal 379 (2020) 122402

Contents lists available at ScienceDirect

Chemical Engineering Journal

journal homepage: www.elsevier.com/locate/cej

Multiple synergistic effects of graphene-based hybrid and hexagonal born nitride in enhancing thermal conductivity and flame retardancy of epoxy

Yuezhan Feng[a,b], Gaojie Han[a], Bo Wang[a], Xingping Zhou[b,*], Jianmin Ma[c], Yunsheng Ye[b,*], Chuntai Liu[a,*], Xiaolin Xie[b]

[a] Key Laboratory of Materials Processing and Mold, Ministry of Education, National Engineering Research Center for Advanced Polymer Processing Technology, Zhengzhou University, Zhengzhou 450002, China
[b] Key Laboratory of Material Chemistry for Energy Conversion and Storage, Ministry of Education, School of Chemistry and Chemical Engineering, Huazhong University of Science and Technology, Wuhan 430074, China
[c] Key Laboratory for Micro-/Nano-Optoelectronic Devices, Ministry of Education, School of Physics and Electronics, Hunan University, Changsha 410022, China

HIGHLIGHTS

- Multiple synergistic effects were employed to prepare high performance PTCs.
- RGO@Ni(OH)$_2$ with multiple flame-retardant effects was used as synergistic filler.
- Synergistic dispersion and bridging connection induce the high heat conduction.
- Catalytic, endothermic, barrier effects contribute to the improved fire resistance.

GRAPHICAL ABSTRACT

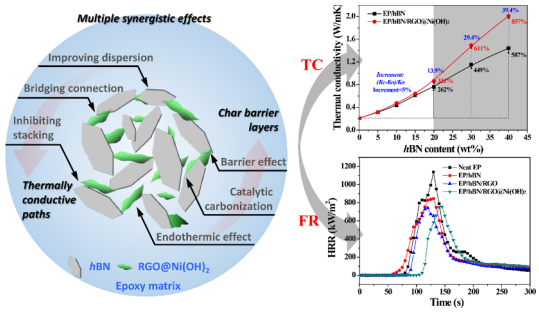

ARTICLE INFO

Keywords:
Synergistic effect
Hexagonal boron nitride
Graphene-based hybrid
Thermal conductivity
Flame retardancy

ABSTRACT

The heat shock, thermal aging and fire hazard of induced by delayed heat diffusion in microelectronic devices require a high-efficiency thermal management system with high-performance electronic packaging materials. In this work, the significant thermal conductivity and flame retardancy of polymer-based thermally conductive composites (PTCs) are addressed by multiple synergistic effects of hexagonal born nitride (*h*BN) and few flame-retardant functionalized graphene. Briefly, a multifunctional hydrophilic graphene-based hybrid containing Ni(OH)$_2$ nanoribbons and reduced graphene oxide (RGO) was synthesized by two-step hydrothermal process. The resulted RGO@Ni(OH)$_2$ hybrid and *h*BN sheets (lateral size of 4.37 ± 1.68 μm and thickness of 80 ± 21 nm) used as synergistic and main fillers, respectively, was simultaneously added into EP matrix. As expected, the binary fillers showed multiple synergistic effects for improving the thermal conductivity and flame retardancy of composites. Typically, the good dispersion and interfacial interaction of RGO@Ni(OH)$_2$ hybrid in matrix can not only inhibit the stacking aggregation behavior of *h*BN sheets, but also bridge adjacent *h*BN sheets, both of which resulted in a high thermal conductivity (2.01 W/mK) of ternary composites with a synergistic increment of 39.4% comparing to EP/*h*BN. On the other hand, their synergistic flame retarding effect including catalytic carbonization, endothermic action and barrier effect induced by RGO@Ni(OH)$_2$, as well as "tortuous path" effect

* Corresponding authors.
E-mail addresses: xpzhou@hust.edu.cn (X. Zhou), ysye@hust.edu.cn (Y. Ye), ctliu@zzu.edu.cn (C. Liu).

https://doi.org/10.1016/j.cej.2019.122402
Received 1 April 2019; Received in revised form 30 July 2019; Accepted 31 July 2019
Available online 01 August 2019
1385-8947/

of *h*BN sheets, jointly led to the formation of a compact and robust char layer in condensed phase during combustion. As a result, EP/*h*BN/RGO@Ni(OH)$_2$ exhibited a desired flame ratardancy with considerable reductions being seen in peak heat release rate, total heat release and total smoke production, *i.e.*, 33.5%, 33.8% and 43.0% comparing to neat EP.

1. Introduction

The continuously increasing heat density in microelectronic devices induced by their miniaturization and integration in modern electronics, makes thermal management system with highly efficient and effective thermal conductive materials be one of the keys to ensuring the working life and safety [1,2]. Polymer-based thermally conductive composites (PTCs) have been widely used as electronic packaging materials to link the heat sources (chips or integrated circuits) and heat sink (or air), because of their light density, low cost, flow processing and high sealing [3–5]. Nevertheless, the intrinsic low thermal conductivity (TC < 0.5 W/mK) and flammability of polymers, as well as the high heat accumulation and loss in electronic packaging materials, inducing the issues of heat shock, thermal aging and fire hazard, severely limited their application in advanced electronic products [6,7]. Consequently, it is hugely desirous to develop a suitable strategy to prepare high-performance PTCs with high TC and flame retardancy, which is significant both in academic research and industrial application.

In general, incorporating inorganic fillers into matrix is main approach to fabricate high-performance polymer composites in industry. Development of high-performance fillers, often determining the final properties, is believed to be the first critical factor for preparing high-performance composites. Recently, two-dimensional (2D) layered materials, such as graphene, hexagonal boron nitride (*h*BN), molybdenum sulfide (MoS_2) *etc.*, have drawn great attention of scientists because of their large specific surface area and attractive properties [8–10]. Among them, as one of the graphene analogs with unique isoelectronic structure, *h*BN shows lots of excellent performances including well in-plane thermal conductivity (200–600 W/mK), ultrahigh electrical insulation and breakdown strength, superb thermal stability and oxidation resistance, outstanding dielectric property and low friction coefficients [11,12]. Combining its high aspect ratio 2D structure, these features make *h*BN as a promising candidate for producing polymer composites with high integrated properties, containing the high TC and flame retardancy [13,14]. However, similar to most of inorganic particles, the poor dispersion and weak interfacial interaction of *h*BN in matrix, resulting in both the degradation of thermally conductive path and the damage the barrier layer during combustion, still limit the further improvement in TC and flame retardancy for PTCs. To solve the issues, surface modification and interlayer exfoliation are considered to be two effective strategies [15–17]. Unfortunately, the very inert surface with less active groups as well as the high strong interlayer interaction of *h*BN seriously restrict the mass-production development of the surface modification and interlayer exfoliation strategies, especially for preparing PTCs with relative high filler loading. Therefore, exploring an effective strategy to improve the dispersion and interfacial interaction of *h*BN remains a formidable challenge for scalable preparation PTCs.

To improve the TC property of PTCs, synergistic effect strategy with the potential in scale-production is often employed both in industry and academia due to its simple and low-cost process [18]. In this strategy, slight easily-dispersed nanofillers, such as graphene oxide (GO), carbon nanotube (CNT), cellulose and their derivatives, are often used to improve the dispersion of TC fillers (*e.g.*, *h*BN [19], Al_2O_3 [6], SiC [20], AlN [21] *etc.*). Zhang et al. [22] revealed that the significant improvement in dispersion of CNT in polymer matrix by adding slight GO, further resulting in the 332% increment for TC property. In addition to this, the intrinsic thermal conductive nanoparticles also act an important bridging joint between TC fillers, resulting in the formation of more efficient TC paths [23]. In this respect, CNT and graphene derivatives with ultrahigh intrinsic TC and aspect ratio can easily connect each other at low filler content. As a result, the significant bridging effects induced by CNT or graphene have been reported to improve the TC property of PTCs in previous literatures [20–25]. For example, the report of Suh et al. [24] revealed an amazing enhancement in TC of epoxy/silver flakes composites (9634% increment from 1.64 to 160 W/mK) by introducing 2.3 vol% silver-functionalized CNTs, where the welding behavior of grafted Ag nanoparticles drastically reinforces the bridging effect of CNTs to enhance both the electronic and lattice (phonon) TC. In view of the arresting action, synergistic dispersion strategy is identified as a feasibly scalable approach to solve the dispersion and interface problems of *h*BN in PTCs.

On the other hand, 2D graphene with surface flame retardant functionalization has been proved to be effective flame retardant additives in improving the fire resistance of polymers without damaging their mechanical and thermal properties, while minimizing environmental disruption when comparing to individual organic or inorganic flame retardants [26,27]. Phosphorus/nitrogen/silicon-containing organics, transition metal oxides, and metal hydroxides have been proved to be as effective synergistic surface modifiers for graphene [28–30]. Their synergistic flame retardation mechanisms including the catalytic carbonization effect, barrier effect, free radical adsorption *etc.*, are believed to contribute the improving flame retardancy. Taking cost, eco-environment, and dispersion into consideration, the hydrophilic transition metal hydroxide (TMH) nanoparticles combining multiple flame-retardant effects of hydroxides and transition metal oxide, including endothermic decomposition reaction of metal hydroxides, catalytic carbonization and smoke suppression effect of transition metal oxides, free radical adsorption ability of its decomposition products (nanoparticles), as well as strong interfacial hydrogen-bond interaction with polymers [31], are believed as the ideal inorganic modifiers [28,32]. Their simple, high-efficiency and eco-friendly wet-chemical synthesis methods of TMH nanoparticles make the mass-production of flame-retardant functionalization graphene to be possible [33,34]. Moreover, comparing to zero/one-dimensional (0D/1D) forms, 2D TMHs (*e.g.*, nanosheets or nanoribbons) with the high aspect ratio and specific area can endow the outstanding dispersion for graphene when hybridizing them. For this reason, the hybridized graphene by 2D THMs has been used as ideal flame retardant additives for polypropylene [28], ABS [35], poly(methyl methacrylate) [36], *etc.* Combining the synergistic enhancement effect in preparing high-performance PTCs, the 2D graphene/THM hybrid is expected to be the well synergistic nanofillers showing multiple synergistic effects with 2D *h*BN both in thermal conductivity, flame retardancy, and other properties.

Our previous works have confirmed the existence of synergistic enhancement effects between graphene and 0D Al_2O_3 particles and 1D silver nanowires in PTCs [6,37]. In contrast, the unique 2D layered structure with high thermal conductivity, stability and oxidation resistance make *h*BN as an ideal candidate in preparing highly thermal conductive and flame retardant PTCs. Therefore, the multiple synergistic effects of 2D *h*BN and graphene are expected to work in improving dispersion, bridging TC paths, flame retardancy, and so on. In this work, 2D Ni(OH)$_2$ nanoribbon with ultrahigh specific surface area and outstanding dispersion was synthesized by one-step hydrothermal process (Scheme 1a), then further used to hybridize with reduced graphene oxide (RGO) by another step hydrothermal process (Scheme 1b). Such the hydrophilic hybrid was used as the synergistic filler to prepare

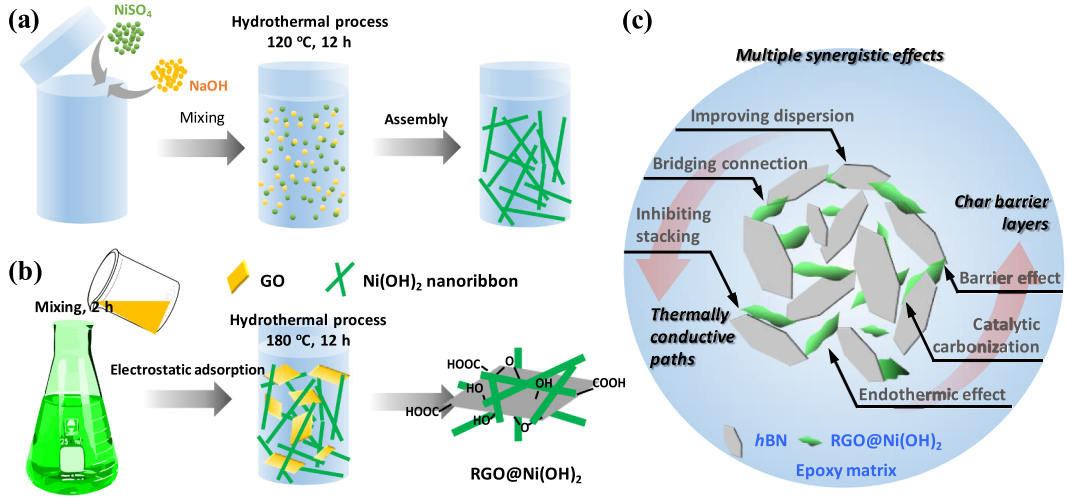

Scheme 1. Illustrations of synthesis routes of (a) $Ni(OH)_2$ nanoribbon and (b) RGO@$Ni(OH)_2$ hybrid by "two-step" hydrothermal process. (c) Multiple synergistic effects of *h*BN and RGO@$Ni(OH)_2$ hybrid in epoxy matrix.

high-performance epoxy/*h*BN composites with simultaneous improvement in TC and flame retardancy via multiple synergistic effects shown in Scheme 1c. The multiple synergistic enhancement mechanisms of thermal conductivity and flame retardancy are also discussed in the context of morphology and char.

2. Experimental section

2.1. Materials

Diglycidyl ether of bisphenol-F epoxy (EP, YDF-170) was supported by KUNDO Chemical Co., Ltd. 2-ethyl-4-methylimidazole (EMI-2, 4, AR) used as cured agent was purchased from Aladdin Industrial Corporation. Nickel sulfate heptahydrate ($NiSO_4{\cdot}7H_2O$), sodium hydroxide (NaOH), ethanol, acetone with analytically reagent were provided by Sinopharm Chemical Reagent Co., Ltd. All chemicals were used without further purification. *h*BN sheets with lateral size range of 5–10 μm were provided by Shanghai Naiou Nano technology Co., Ltd. Graphene oxide (GO) was prepared by chemically exfoliating natural graphite based on our previous work [6].

2.2. Synthesis of $Ni(OH)_2$ nanoribbons

$Ni(OH)_2$ nanoribbon was synthesized by a simple hydrothermal process based on previous literatures [33,38], as shown in Scheme 1a. Typically, $NiSO_4$ aqueous solution (300 mL/117.6 mmol) was firstly prepared, and following with slowly adding NaOH aqueous solution (180 mL/58.8 mmol) with vigorous stirring, to prevent flocculation. The solution was further stirred for 2 h, then transferred to five 50 mL Teflon-lined autoclaves to suffer an inclosed hydrothermal process at 120 °C for 12 h. After that, the obtained products ($Ni(OH)_2$ nanoribbon) were filtered and washed with deionized water for several times, stored in aqueous solution with a concentration of 10 mg/mL.

2.3. Preparation of RGO@$Ni(OH)_2$ hybrid

Electrostatic self-assembly was employed to prepare RGO@$Ni(OH)_2$ hybrid via a further hydrothermal process (Scheme 1b). In brief, GO aqueous solution was slowly added into the $Ni(OH)_2$ nanoribbon aqueous solution with the GO:$Ni(OH)_2$ mass ratio of 1:1 under a vigorous stirring. The concentration of GO was diluted to 2 mg/mL with a sufficient stirring for 2 h. Then the solution was transferred to 50 mL Teflon autoclaves, and heated to 180 °C for 12 h. During this hydrothermal process GO sheets were synchronously reduced and coated with Ni$(OH)_2$ nanoribbons. Finally, the resultant gel-like products (RGO@Ni$(OH)_2$ hybrid) were ultrasonic-broken, filtered and washed with deionized water for several times in deionized water. The purified RGO@Ni$(OH)_2$ hybrid was stored in ethanol solution with a concentration of 10 mg/mL.

2.4. Fabrication of EP/hBN/RGO@$Ni(OH)_2$ composites

In a typical procedure, the ethanol solution of RGO@$Ni(OH)_2$ hybrid was firstly ultrasonic-mixed with stoichiometric EP monomers solution in acetone for 1 h. Then the bulk of mixed solvent was rapidly removed using a rotary evaporator. Afterwards *h*BN sheets were uniformly dispersed into the above-mentioned obtained mixture by using a planetary stirrer. The resulted EP/*h*BN/RGO@$Ni(OH)_2$ mixture was dried and outgassed in vacuum at 60 °C for 12 h, and following with adding 6 wt% EMI-2,4 (curing agent). Finally, the composite was cured according to a programmed-temperature of 60 °C for 2 h, 100 °C for 2 h and 150 °C for 5 h. The content of RGO or RGO@$Ni(OH)_2$ were fixed as 2 wt% relative to EP, and *h*BN sheets showed a concentration variation of 5, 10, 15, 20, 30 and 40 wt% relative to composites. For comparison, EP/*h*BN and EP/*h*BN/RGO composites were fabricated using the same process.

2.5. Characterizations

X-ray diffraction (XRD) patterns were carried out on a PANalytical X'Pert PRO diffractometer equipped with a Cu-Kα radiation (λ = 0.154 nm). Laser-Raman scattering analyses were executed on a LabRAM HR800 Raman spectrometer with 532 nm Nd laser. Fourier transform infrared spectra (FTIR) were recorded by using a Bruker Equinox 55 FTIR spectrometer with KBr pellet. X-ray photoelectron spectroscopy (XPS) was performed on a Shimadzu-Kratos AXIS-ILTRA DLD-600 W spectrometer using an Al Kα anode. Transmission electron microscopy (TEM) and scanning electron microscopy (SEM) images were obtained by using Tecnai G2 20 S-TWIN TEM and FEI Nova NanoSEM450 field emission SEM with an acceleration voltage of 200 and 10 kV, respectively. Energy disperse X-ray spectroscopy (EDX) was simultaneously conducted with SEM measurements. Thermogravimetric analyses (TGA) were tested on a Perkin Elmer TGA 4000 equipment with a heating rate of 10 °C/min.

The TC values of composites were measured via hot-wire method with a KEM QTM-500 Quick Thermal Conductivity Meter at room temperature based on ASTM C1113 90 standard. The combustion behaviors of composites were analyzed based on limiting oxygen index

(LOI), UL-94 vertical burning, and cone calorimeter (CC) measurements. The rectangular specimens for LOI (100 × 6.5 × 3 mm^3), UL-94 (100 × 13 × 3 mm^3) and CC (100 × 100 × 3 mm^3) were examined on HC-2 oxygen index meter, CZF-3 horizontal vertical combustion apparatus, and FTT cone calorimeter, based on GB/T 2405–2009, GB/T 2408–2008, and GB/T 16172–2007, respectively.

3. Results and discussion

3.1. Characterizations of RGO@Ni(OH)$_2$ hybrid

It is well-known that the main flame retardant mechanism of inorganic hydroxide is the cooling effect of its endothermic decomposition reaction [39]. As shown in Fig. S1, the TGA curve of Ni(OH)$_2$ under air atmosphere reveals the two-step thermal decomposition behavior at 200–400 °C and 600–700 °C, respectively, corresponding to its thermal decomposition with products of water and Ni_2O_3 and the further oxidation of NiO [40,41]. The corresponding DSC pattern confirms the decomposition endothermic peaks at 263 °C (0.337 W/g) and 374 °C (0.872 W/g). Moreover, the catalytic carbonization and free radical adsorption ability of NiO nanoparticles make Ni(OH)$_2$ have outstanding flame retardant effect, which were thus chosen to functionalized RGO in this work.

Ni(OH)$_2$ nanoribbon synthesized by one-step hydrothermal process, is suitable to functionalize RGO due to its more specific surface area and aspect ratio when comparing to nanoparticle, nanowire, or nanoplate. TEM image of Ni(OH)$_2$ (Fig. 1a) confirms ribbon-like morphology with a width of 15–20 nm and a length of 1–2 μm. Such Ni(OH)$_2$ nanoribbons can be easily adhered onto RGO's surface by electrostatic interaction during a further hydrothermal process. In comparison to the

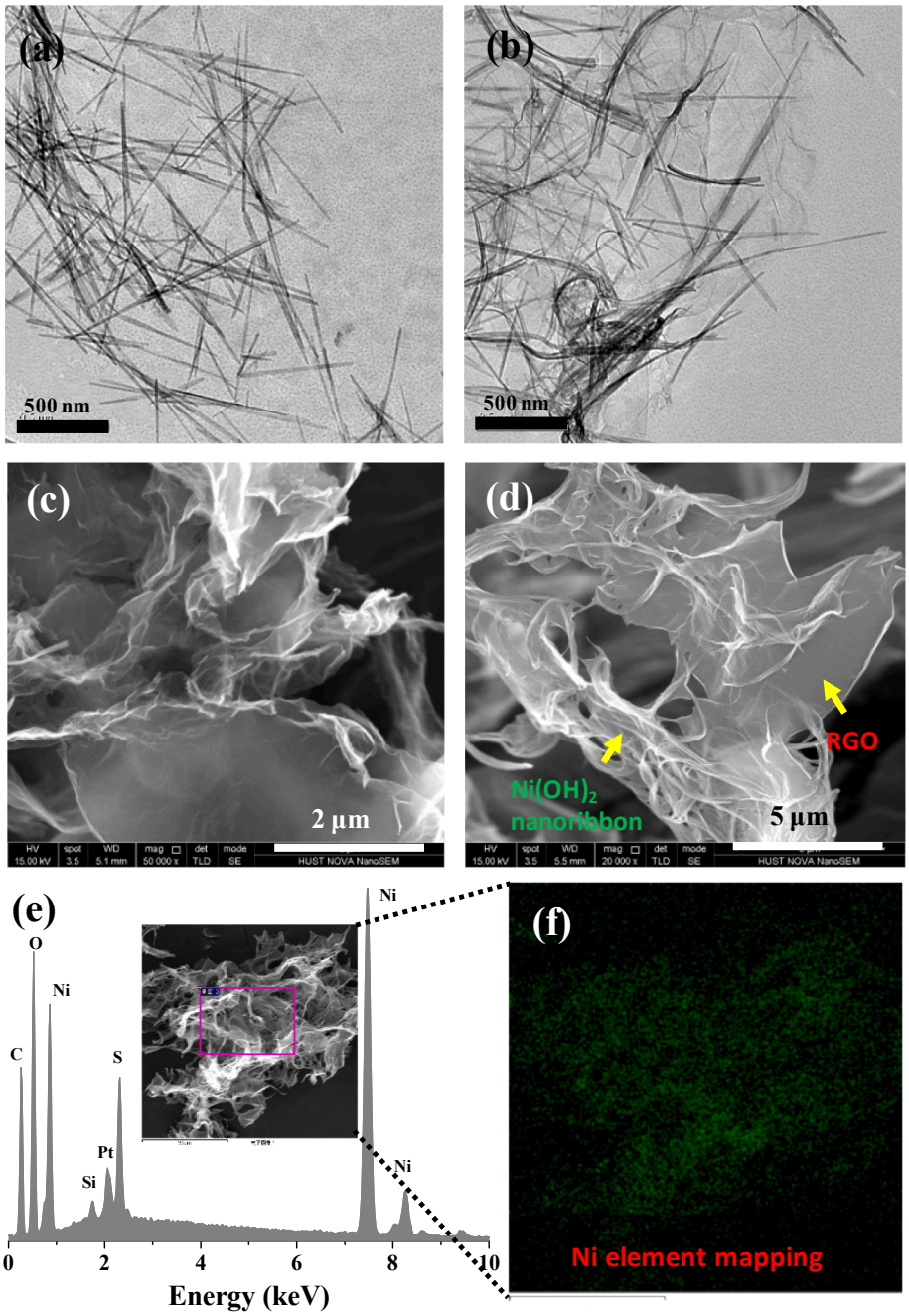

Fig. 1. TEM images of (a) Ni(OH)$_2$ nanoribbon and (b) RGO@Ni(OH)$_2$ hybrid; SEM images of (c) RGO and (d) RGO@Ni(OH)$_2$ hybrid; (e) EDX spectrum and (f) Ni element mapping of RGO@Ni(OH)$_2$ hybrid.

transparent and smooth with few flexible wrinkles of RGO sheets reduced by the same hydrothermal process (Fig. S2 and Fig. 1b), the morphology of RGO@Ni(OH)$_2$ hybrid (Fig. 1c and d) exhibits that Ni(OH)$_2$ nanoribbons closely adhere to RGO sheets without any stacking phenomenon. The EDX spectrum and Ni element mapping (Fig. 1e and f) reveal that abundant Ni element uniformly distributes on the surface of RGO@Ni(OH)$_2$ hybrid, also confirming the Ni(OH)$_2$ flame-retardant functionalized RGO. Moreover, the strong interaction between RGO and Ni(OH)$_2$ can stand against ultrasonic treatment more than 10 min without shedding nanoribbons observed during TEM test.

The crystal structures of RGO@Ni(OH)$_2$ hybrid were confirmed by powder XRD technique. As shown in Fig. 2a, when comparing to natural graphite [6], the (0 0 2) diffraction peak of graphitic lattice shifts to $2\theta = 11.8^{\circ}$ with a *d*-spacing of 0.75 nm after oxidation, because of the intercalation of oxygen-containing groups [42]. The reduction by hydrothermal process can eliminate most of oxygen-containing groups in GO, and results in the shift of the (0 0 2) peak to $2\theta = 23.6^{\circ}$ with a broad band form. Ni(OH)$_2$ nanoribbon displays six strong diffraction peaks at $2\theta = 12.9^{\circ}$, 17.4°, 23.0°, 30.3°, 40.4° and 45.6° in its XRD diffraction pattern, respectively, corresponding to the (0 0 2), (1 0 2), (2 0 1), (2 0 3), (0 1 4), (1 0 1) and (4 0 0) lattice planes of monoclinic α-Ni(OH)$_2$ based on JCPDF No. 41-1424 [43,44]. All of diffraction peaks of α-Ni(OH)$_2$ are observed on the XRD diffractogram of RGO@Ni(OH)$_2$ at same location, further demonstrating that Ni(OH)$_2$ nanoribbon was coated onto the surface of RGO successfully. Meanwhile, the complete disappearance of (0 0 2) diffraction peak in RGO@Ni(OH)$_2$ hybrid means the effective suppression for the restacking of RGO sheets by coating Ni(OH)$_2$ nanoribbon.

Fig. 2b exhibits the Raman spectra of Ni(OH)$_2$, GO, RGO and RGO@Ni(OH)$_2$ hybrid. Two characteristic peaks at ~1334 (*D* band) and 1573 cm^{-1} (*G* band) of graphitic structure, corresponding to the A_{1g} breathing mode of sp^3 carbon in disorder/defect domains, and the E_{2g}-vibration mode of sp^2 carbon in graphitic lattice domains [45], are observed in all graphene derivatives. In contrast to GO and RGO, *D* and *G* bands show a tiny red-shift in RGO@Ni(OH)$_2$ hybrid due to the charge transfer between RGO and Ni(OH)$_2$. The new peaks around 450, 480 and 1004 cm^{-1}, belonging to Ni(OH)$_2$, are found in the spectrum of RGO@Ni(OH)$_2$ hybrid, re-confirming the successful Ni(OH)$_2$ flame-retardant functionalization for RGO. Additionally, the intensity ratio of *D* and *G* band (I_D/I_G) presents a little change after reduction or functionalization, which means that little lattice damage happened during the hydrothermal process.

In this work, only electrostatic interaction is hard to keep its structural integrity after suffering ultrasonic treatment as described in TEM section. For this reason, FTIR and XPS techniques were employed to verify the interaction between RGO and Ni(OH)$_2$ nanoribbon in RGO@Ni(OH)$_2$ hybrid. The new absorption peaks at 702 and 3602 cm^{-1} belonging to the Ni-O band and hydroxyl stretching vibration of Ni(OH)$_2$ nanoribbon are found in RGO@Ni(OH)$_2$ hybrid FTIR spectra (Fig. 2c). The strong hydrogen-bond interaction between hydroxide and carboxyl of GO can be proved according to the obvious shift of carboxyl peak shifts to 1654 cm^{-1} when comparing to GO (1734 cm^{-1}). Furthermore, a significant proof of the sharp peak at 1101 cm^{-1}, attributing to C–O–Ni bond, proves the presence of covalent linking in our hybrid. Therefore, both hydrogen-bond interaction and covalent linking make Ni(OH)$_2$ nanoribbon to adhere on the surface of RGO closely.

Fig. 2d-e present the XPS spectra of Ni(OH)$_2$, RGO and RGO@Ni(OH)$_2$ hybrid, to further confirm the covalent linking. The characteristic peaks of Ni(OH)$_2$ and RGO are observed on RGO@Ni(OH)$_2$ hybrid spectrum. In contrast, the reducing C/O atomic ratio of hybrid is ascribed to the introducing O element by Ni(OH)$_2$ coating. The high-resolution spectrum at Ni 2p region (inset in Fig. 2d) reveals two main spin-orbital splitting peaks of Ni 2p$_{1/2}$ and Ni 2p$_{3/2}$ at 874.4 and 856.6 eV with a spin-energy separation of 17.8 eV, which is the characteristic of α-Ni(OH)$_2$ [46]. The C 1s core-level XPS spectra of RGO and RGO@Ni(OH)$_2$ (Fig. 2e) show six fitting peaks at same location, which can be attributed to sp^3 C (284.5 eV), sp^2 C (285.0 eV), C-OH (285.6 eV), C–O–C (286.9 eV), C═O (287.5 eV) and C(O)OH (289.0 eV), respectively, based on the our previous report [47]. In contrast, RGO@Ni(OH)$_2$ hybrid exhibits a more intensive C-OH fitting peak at 285.6 eV because of the presence of hydrogen-bond interaction. A noticeable difference induced by functionalization can be found in O 1s region. As shown in Fig. 2f, the high-resolution O 1s spectrum of

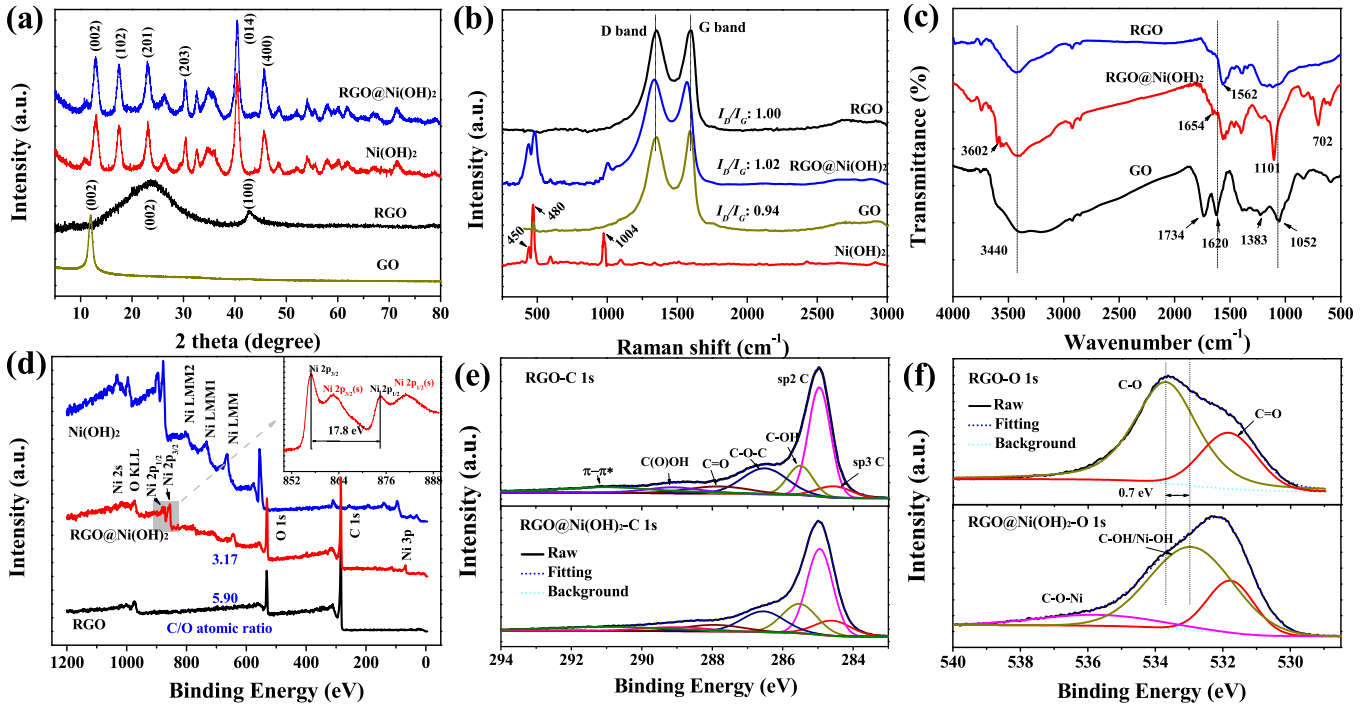

Fig. 2. (a) XRD diffractograms, and (b) Raman, (c) FTIR, (d) XPS spectra of GO, RGO, Ni(OH)$_2$ nanoribbon and RGO@Ni(OH)$_2$ hybrid; High-resolution XPS spectra of RGO and RGO@Ni(OH)$_2$ hybrid at (e) C 1s and (f) O 1s regions.

RGO show two fitting peaks at 531.9 and 533.7 eV, respectively, belonging to the double and single bonds linking with graphitic lattice. For RGO@$Ni(OH)_2$ hybrid, the C-O-Ni fitting peak at 535.8 eV, proving the presence of covalent linking, is observed in its O 1s region. The C-OH fitting peak shifts to low-energy region about 0.7 eV by coating $Ni(OH)_2$ nanoribbon.

TGA is a powerful tool to explore the functionalization and estimate flame-retardant efficiency of graphene derivatives. As presented in Fig. 3, GO exhibits a continuous thermal decomposition before 150 °C with ~12% weight loss and a sharp down stage between 200 and 300 °C with ~30% weight loss, corresponding to its absorbed water and non-stable oxygen-containing groups, respectively [48]. After removing the most oxygenated functional groups during hydrothermal reduction process, the drastic thermal decomposition at low temperature (< 400 °C) is suppressed and ~7% continuous weight loss during this stage is associated with residual oxygenated groups. However, the excessive existence of sp^2 carbon due to relatively weak reduction results in the unstable carbonaceous structure in RGO with poor thermal stability under high temperature. During TGA testing, the RGO shows a rapid weight loss corresponding to the pyrolysis of unstable carbonaceous structure after 500 °C [8]. By comparison, RGO@$Ni(OH)_2$ hybrid exhibits two thermal decomposition stages at 200–400 °C and 500–600 °C, respectively, which are almost consistent with the thermal decomposition process of $Ni(OH)_2$ nanoribbon describing in above section (Fig. S1). In view of the thermal decomposition behaviors of RGO and $Ni(OH)_2$, the two decomposition stages of hybrid can be ascribed to the superposition of the decomposition of $Ni(OH)_2$ and RGO, where Ni_2O_3 and NiO nanoparticles are produced in the RGO hybrid during the two stages, respectively. Additionally, Ni nanoparticles may be obtained due to the weak reducing ability of graphene for $Ni(OH)_2$ nanoribbons under high temperature [49]. Moreover, the appearance of a plateau corresponding to 42.5 wt% residues in hybrid's TGA curve beyond 700 °C, comparing to the continuous weight loss of RGO, means that carbonaceous structure of RGO at high-temperature was effectively reinforced by adherent $Ni(OH)_2$ nanoribbons. Therefore, the decomposed products (NiO and Ni nanoparticles), as well as reinforced carbonaceous structure of RGO would play an important role when as a flame retardant additive for polymers.

3.2. Morphology and structure of EP/hBN/RGO@$Ni(OH)_2$ composites

As mentioned above, the multiple flame retardant mechanisms including cooling effect, catalytic carbonization and free radical absorption of $Ni(OH)_2$ nanoribbon and its decomposition products, can effectively increase the flame retardant efficiency of RGO@$Ni(OH)_2$ hybrid. On the other hand, the hydrogen-bond interaction between Ni $(OH)_2$ and polar functional groups in polymers can also improve the interfacial interaction between RGO and matrix [31]. As exhibited in Fig. 4a, RGO sheets show a very poor dispersion in EP matrix and weak interfacial interaction with remarkable gaps (red circle in Fig. 4a) between RGO and matrix. After functionalization with $Ni(OH)_2$ nanoribbon, the presence of strong hydrogen-bond interaction between Ni $(OH)_2$ and imidazole groups in EP matrix leads to the effective suppression for the restacking of RGO, resulting in that no RGO aggregations were found on the fracture surface of EP/RGO@$Ni(OH)_2$. Moreover, the relatively ductile fracture of EP/RGO@$Ni(OH)_2$ (see Fig. 4b) with rough surface and plenty of cracks also confirms the significant improvement in the dispersion and interfacial interaction of RGO in the matrix.

In this work, 2D *h*BN sheets with a mean lateral size of 4.37 ± 1.68 μm and thickness of 80 ± 21 nm (Fig. S3) are chosen as the conductive filler due to its high aspect ratio, electric insulation, ultrahigh chemical and thermal resistance. The multiple synergistic effects between *h*BN and RGO@$Ni(OH)_2$ hybrid are used to enhance the TC and flame retardancy of EP-based composites, which are importantly impacted by the dispersion, distribution, and interfacial interaction of fillers. In low magnification SEM images (Fig. S4, Fig. 4c and e), the fracture surfaces of all composites reveal the relatively uniform distribution of *h*BN without obvious defects or holes in whole region. However, due to gravity action, 2D *h*BN micro-sheets tend to stack along in-plane during curing process in EP/*h*BN composites, especially for the composites with high filler loading (20 and 40 wt%, Figs. 4c and S4), which severely weakens the final properties in through-plane [50]. After further incorporating RGO@$Ni(OH)_2$ hybrid in EP/*h*BN composites, such stacking behavior is effectively suppressed by increasing the viscosity of curing system, which is profound for the improvement in through-plane TC. Moreover, the suppression effect can be further confirmed by XRD technique due to the sharp difference between the diffracted intensity of (0 0 2) and (1 0 0) lattice plane of *h*BN (Fig. S5) [51]. In addition, the high magnification SEM images (red arrows in Fig. 4d and red circles in Fig. S6) reveal that *h*BN sheets exhibit stacked aggregation distribution in EP/*h*BN composites, with noticeable gaps are observed in the *h*BN aggregations. In contrast, the stacking aggregation behavior of *h*BN sheets can be effectively restrained when adding RGO@$Ni(OH)_2$ hybrid in composites, where *h*BN sheets (red arrows in Figs. 4f and S6) are almost monodisperse in matrix. Moreover, the existing RGO@$Ni(OH)_2$ hybrid between adjacent *h*BN sheets can also acts as a bridge linking *h*BN sheets, resulting in the formation of continuous thermal conductive network.

3.3. Thermal conductivity of EP/hBN/RGO@$Ni(OH)_2$ composites

The values of TC for EP/*h*BN/RGO@$Ni(OH)_2$ composites were measured by steady-state hot-wire method, and the results are shown in Fig. 5a. Neat EP shows a relatively low TC of 0.21 W/mK due to the lack of conductive path for phonon or electron. Incorporating a large number of *h*BN sheets into EP matrix can induce the formation of inorganic filler network, which allows phonons (heat carrier) to transmit the EP matrix quickly, resulting in the obvious improvement in TC property of EP/*h*BN composites. For example, the TC enhancement (TCE, comparing to neat EP) of composites at 20, 30 and 40 wt% *h*BN are 262, 449, 587%, respectively. Even so, the synergistic effect between 2D graphene and *h*BN is expected to further enhance the values of TC as our previous reports [6,37]. As a result, when adding 2 wt% RGO@$Ni(OH)_2$ hybrid into EP/*h*BN composites, the TC values show an interesting change as function of *h*BN loading, *i.e.,* showing a negligible improvement below 20 wt% loading compared to the corresponding EP/*h*BN, but an ever-increasing synergistic enhancement beyond 20 wt % loading, due to the increasing inter-particle interactions. Defining $(K_{c1} - K_{c0})/K_{c0}$ as the strength of the synergistic effect, where K_{c1} and K_{c0} are the TC of EP/*h*BN/RGO@$Ni(OH)_2$ and EP/*h*BN, respectively. As presented in Fig. 5a, the synergistic effect strength is below 5% at 5, 10

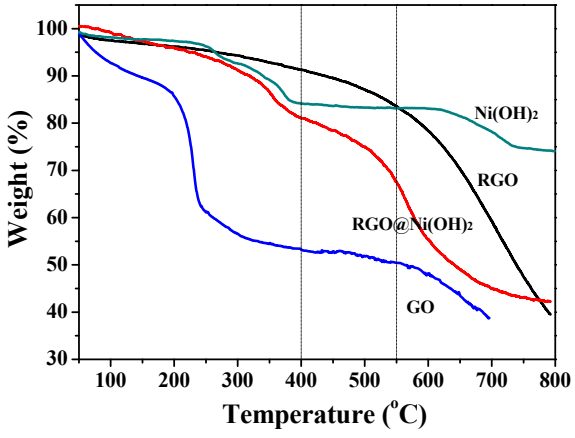

Fig. 3. TGA curves of GO, RGO, $Ni(OH)_2$ nanoribbon and RGO@$Ni(OH)_2$ hybrid under nitrogen atmosphere.

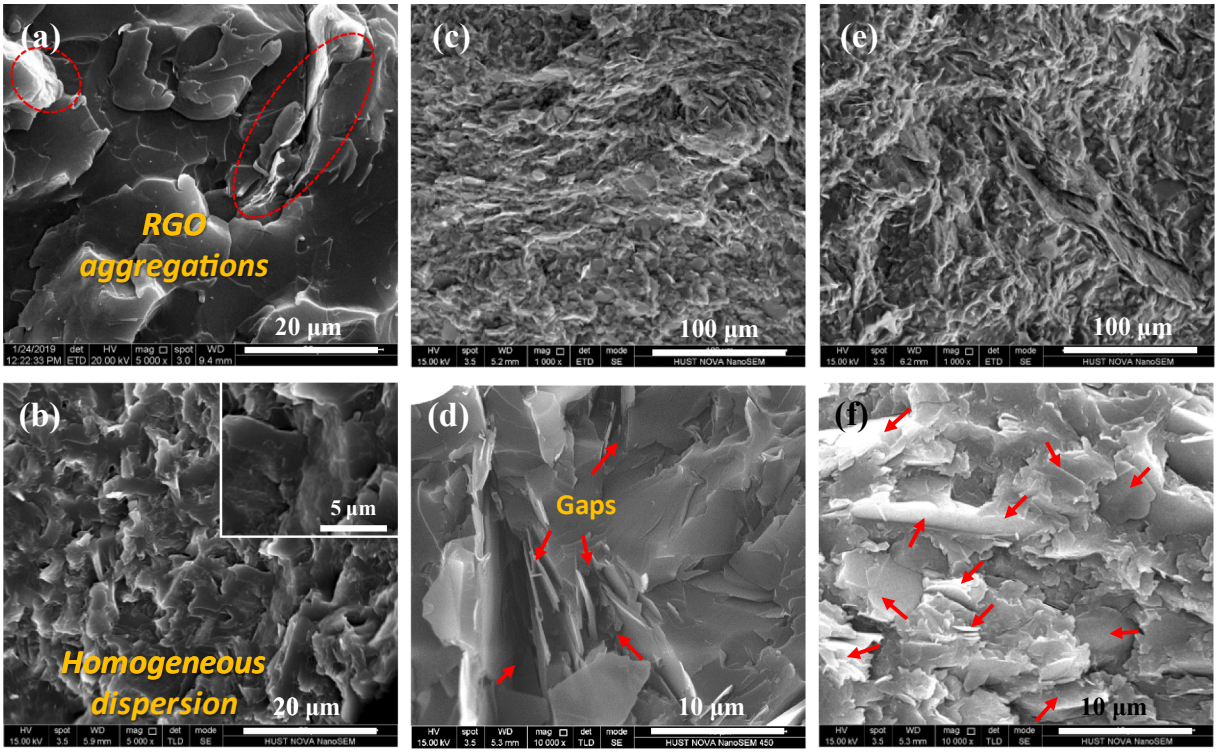

Fig. 4. SEM images for the fracture surface of (a) EP/RGO, (b) EP/RGO@Ni(OH)$_2$, (c, d) EP/*h*BN and (e, f) EP/*h*BN/RGO@Ni(OH)$_2$ with 20 wt% *h*BN sheets.

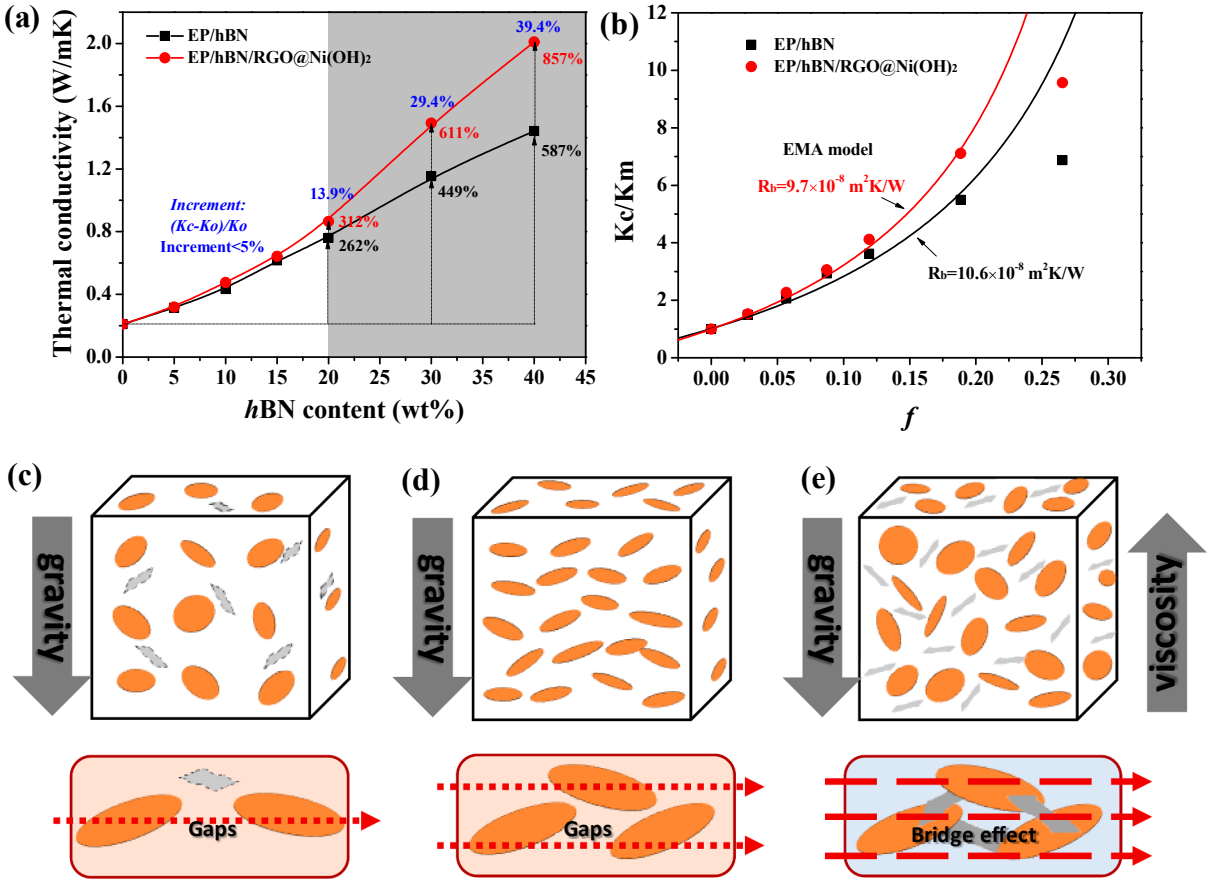

Fig. 5. (a) Thermal conductivity of EP/*h*BN and EP/*h*BN/RGO@Ni(OH)$_2$ composites as a function of *h*BN content; (b) the model fitting curves (lines) to the corresponding experimental data (dots); the proposed thermal conductive models for (c) EP/*h*BN or EP/*h*BN/RGO@Ni(OH)$_2$ with low *h*BN loading, (d) EP/*h*BN and (e) EP/*h*BN/RGO@Ni(OH)$_2$ with high *h*BN loading.

and 15 wt% *h*BN loading, while the values are 13.9, 29.4 and 39.4% when increasing the filler loading to 20, 30 and 40 wt%, respectively, which is consistent with previous work [52].

Our previous works revealed that the decreasing interfacial thermal resistance (R_b) induced by adding flame-retardant functionalized graphene is one of main reason for the improving TC of EP/Al_2O_3 and EP/silver nanowires composites [6,37]. Herein, effective medium approximation (EMA) theory [53] is also employed to calculate change of R_b between *h*BN sheets and EP matrix induced by incorporating RGO@Ni(OH)$_2$ hybrid. For homogeneous phase system containing 2D fillers, Nan et al. [54] developed a universal formula based EMA model as following:

$$\frac{K_c}{K_m} = \frac{3 + f[2\beta_{11}(1 - L_{11}) + \beta_{33}(1 - L_{33})]}{3 - f[2\beta_{11}L_{11} + \beta_{33}L_{33}]} \quad (1)$$

$$L_{11} = L_{22} = \frac{p^2}{2(p^2 - 1)} + \frac{p}{2(1 - p^2)^{3/2}}\cos^{-1}p \quad (2)$$

$$L_{33} = 1 - 2L_{11} \quad (p < 1) \quad (3)$$

$$\beta_{ii} = \frac{K_{ii}^c - K_m}{K_m + L_{ii}(K_{ii}^c - K_m)} \quad (4)$$

$$K_{ii}^c = \frac{K_p}{1 + \frac{\gamma L_{ii} K_p}{K_m}} \quad (5)$$

where $\gamma = (1 + 2p)\alpha$, $\alpha = \frac{R_b K_m}{a}$, K_c, K_m and K_p are the TC of composites, matrix and fillers, respectively. f is volume fraction. L_{ii} is geometrical factor dependent on the shape of particles. K_{ii}^c is the equivalent TC along symmetric axis of the composite unit cell. p and a is the reciprocal of aspect ratio and thickness of filler, respectively. In EP/*h*BN and EP/*h*BN/RGO@Ni(OH)$_2$ composites, *h*BN sheets with aspect ratio of ~300 (Fig. S3) and TC of 360 W/mK were used as TC filler, for simplicity, the other parts (EP or EP/RGO@Ni(OH)$_2$) of the composites were regarded as matrix with K_m of 0.210 and 0.231 W/mK, respectively. Fitting the experimental data based on Eqs. (1)–(5), the results are shown in Fig. 5b. It should be pointed out that EMA model is only suitable to the system with low filler loading due to the assumption of no particle interaction and no clustering. Therefore, only the data below 30 wt% *h*BN loading are well-fitted in this work. The fitting results demonstrate that the similar R_b in EP/*h*BN (10.6×10^{-8} m^{2}K/W) and EP/*h*BN/RGO@Ni(OH)$_2$ (9.7×10^{-8} m^{2}K/W) composites, indicating that the introducing RGO@Ni(OH)$_2$ hybrid shows a very weak effect on the R_b at low filler loading.

Synergetic enhancement effects in TC by multiple fillers are well-known in previous reports, such as improving dispersion and interfacial interaction, bridging effect and so on [23,55]. Based on the morphology analysis and the TC data of composites, the synergetic effect on the TC of EP/*h*BN/RGO@Ni(OH)$_2$ can be discussed as two parts. For the composites with low *h*BN loading, as shown in Fig. 5c, the "dilute" *h*BN sheets in matrix is hard to be affected by adding small amount RGO@Ni(OH)$_2$ hybrid because of the weak interaction between the two fillers. Although the dispersion of *h*BN sheets is improved to some extend, the discontinuous thermal conductive paths still induce the low TC in EP/*h*BN/RGO@Ni(OH)$_2$. Concerning high loading composites, the stacking and aggregation behaviors of *h*BN sheets and the existing gaps between adjacent *h*BN sheets result in the relatively low TC in though-plane direction of EP/*h*BN (Fig. 5d). Such behaviors can be effectively suppressed by further adding RGO@Ni(OH)$_2$ hybrid into EP/*h*BN (high filler loading) due to the increasing the viscosity of composite slurry as

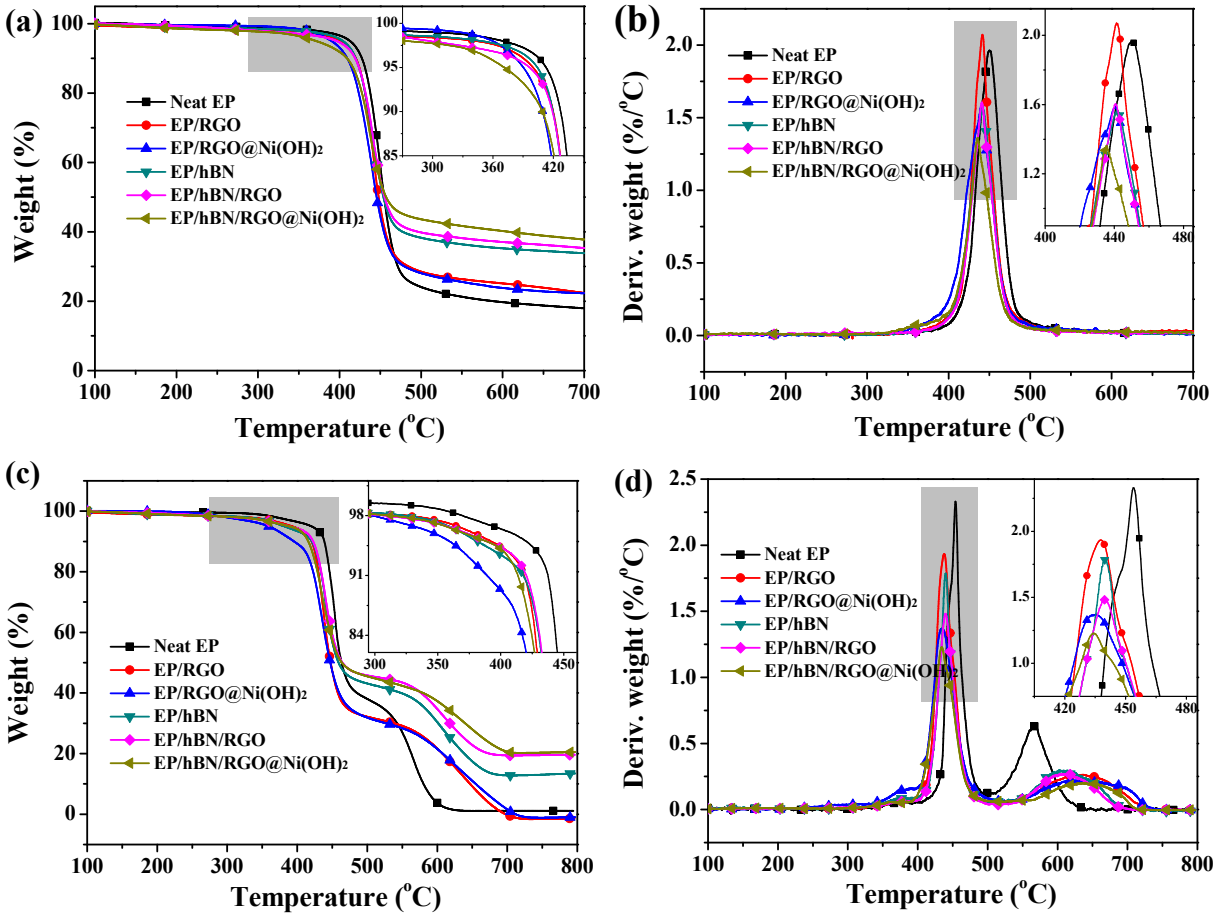

Fig. 6. TGA and DTG curves of neat EP and its composites with 2 wt% graphene and/or 20 wt% *h*BN under (a, b) nitrogen and (c, d) air atmosphere.

described above (Fig. 5e). Combining with the bridging connection of graphene, a continuous and efficient thermal conductive network can be formed in EP/*h*BN/RGO@Ni(OH)$_2$, which results in the strong synergetic enhancement effect on TC of the composites at high *h*BN loading.

3.4. Thermal stability and flame retardancy of EP/hBN/RGO@Ni(OH)$_2$ composites

The significant thermal (oxidative) stability of EP-based composites, to reveal the thermal decomposition and combustion behaviors, is given in Fig. 6. Neat EP shows one-stage thermal degradation corresponding to the pyrolysis of epoxy chains (400–500 °C) in nitrogen atmosphere, and the other mass-loss stage (500–700 °C) belonging to the oxidation of chars when existing oxygen during thermal decomposition [29,47]. In contrast to neat EP, EP/*h*BN exhibits a lower onset thermal decomposition temperature (T_{onset}) due to the presence of a mass of high thermal conductive *h*BN sheets, which means the easy and quick heat absorption of composites. However, the "tortuous path" effect of 2D *h*BN sheets, which hinders the transfer of volatile products [56], results in the obvious reduction in mass loss rate, and the large improvement of char yield. Moreover, the char's pyrolysis is also delayed drastically, which means the obviously increasing oxidation resistance of chars. When incorporating 2 wt% RGO or RGO@Ni(OH)$_2$ hybrid into EP or EP/*h*BN composite, all the resulted composites demonstrates a decreasing T_{onset} due to the thermally nonstable RGO and RGO@Ni(OH)$_2$ hybrid (Fig. 3). The incorporated RGO composites with poor dispersion and interfacial interaction present increasing mass loss rate comparing to their matrix (EP or EP/*h*BN). By comparison, the multiple effects of RGO@Ni(OH)$_2$ hybrid including endothermic decomposition of Ni(OH)$_2$ nanoribbon, catalytic carbonization and free radical adsorption of NiO/Ni nanoparticles, as well as the well-disperse graphene with strong interfacial interaction with EP matrix, result in the improvement of their thermal decomposition behavior in terms of decreasing mass loss rate, improving char yield and increasing chars' oxidation resistance. Combining with the "tortuous path" effect of *h*BN sheets, a more effective protective barrier layer containing more organic carbides, graphene and *h*BN sheets can be formed in EP/*h*BN/RGO@Ni(OH)$_2$ composite during thermal degradation, which leads to the remarkable improvement in its thermal (oxidative) stability.

Cone calorimeter (CC), limit oxygen index (LOI) and UL-94 vertical burning tests were employed to detect the synergistic resistance effect of *h*BN and RGO@Ni(OH)$_2$ hybrid on the flammability of EP in bench-scale tests under real-world fire conditions [57]. Fig. 7 gives the relation curves of heat release rate (HRR), total heat release (THR), total smoke production (TSP) and mass loss versus time, and their corresponding combustion parameters are listed in Table 1. Neat EP demonstrates high flammable features of easy ignition, rapid burning, high heat release and dense smoke during continuous heat radiation of CC test, with low time to ignition (TTI) of 67s, high peak heat release rate (PHRR) of 1137.6 kW/m^2, THR of 81.6 MJ/m^2 and TSP of 62.4 m^2. Moreover, EP sample with low LOI value of 25.0 vol% can burn continuously with a plenty of drippings during UL-94 vertical burning test (NR). RGO or RGO@Ni(OH)$_2$ hybrid used as flame retardant additives in this work can decrease the combustibility of EP at a certain extent. In contrast, the multiple flame retardant effects of the hybrid, as well as its well dispersion and interfacial interaction in matrix, lead to a better flame retardance of EP/RGO@Ni(OH)$_2$ composite. The corresponding HRR, THR and TSP values fall by 31.6%, 8.6% and 7.9% comparing to neat EP, respectively. Moreover, the composite also passed the UL-94V-

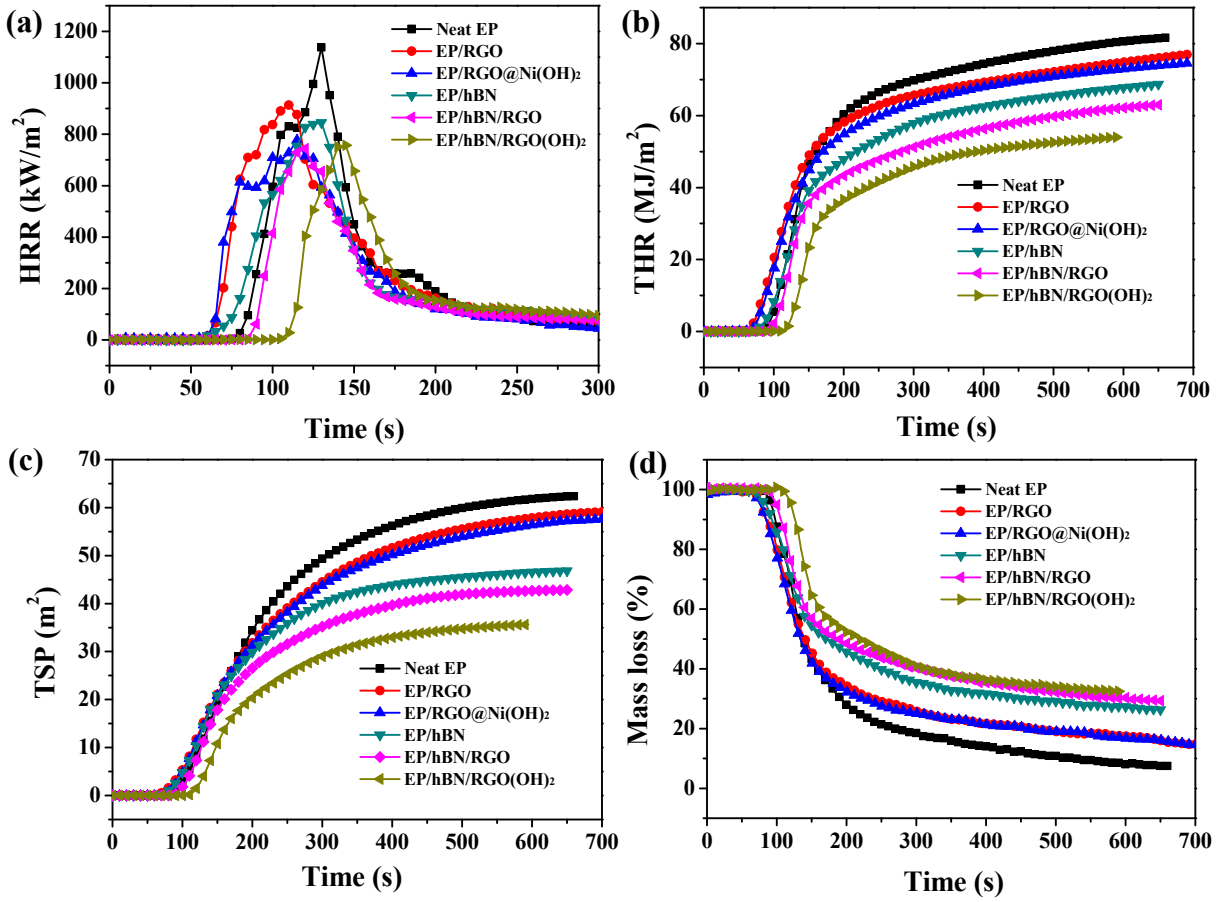

Fig. 7. (a) Heat release rate, (b) total heat release, (c) total smoke production rate and (d) mass loss versus time curves of neat EP and its composites with 20 wt% *h*BN and 2 wt% graphene.

Table 1
Combustion data of neat EP and its composites.

Samples	TTI (s)	PHRR (kW/m^2)	THR (MJ/m^2)	TSP (m^2)	FIGRA (kW/m^{2}s)	LOI (vol %)	UL-94 rating
Neat EP	67	1137.6	81.6	62.4	8.8	25.0	NR
EP/RGO	57	913.7	77.0	59.1	8.3	24.7	NR
EP/RGO@Ni(OH)$_2$	55	777.7	74.6	57.5	6.8	26.6	V-2
EP/*h*BN	45	845.3	68.7	46.8	6.5	27.2	NR
EP/*h*BN/RGO	80	743.7	63.0	42.8	6.2	28.0	V-2
EP/*h*BN/RGO@Ni(OH)$_2$	103	756.8a	54.0	35.6	5.2	29.2	V-1

2 testing with an increased LOI value of 26.6 vol%. For the PTCs in this work, adding *h*BN sheets (20 wt%) into EP matrix can induce the effective improvement in its flammability including PHRR (845.3 kW/m^2), THR (68.7 MJ/m^2) and TSP (46.8 m^2), corresponding to the reduction of 25.7%, 15.8% and 25.0%, respectively. Meanwhile, the disappearance of char combustion exothermic peak at 150–200 s in HRR curve (Fig. 7a) comparing to neat EP indicates the increased oxidation resistance of chars in EP/*h*BN, which is agreed with the TGA analysis. However, the high TC and the relative low melt viscosity results in the decreasing TTI for EP/*h*BN (45 s), which means the ease of ignition during a fire hazard [47]. Besides, EP/*h*BN shows some improvement in LOI to 27.2 vol%, but still can't pass UL-94 testing. As synergistic fillers, RGO and RGO@Ni(OH)$_2$ hybrids are expected to further improve the flame retardancy of EP/*h*BN in this work. The results reveal that RGO shows a very low synergistic flame retardant effect due to its low catalytic carbonization ability, poor dispersion and weak interfacial interaction in EP/*h*BN matrix. By comparison, coating Ni(OH)$_2$ nanoribbon onto RGO sheets can effectively improve their interfacial compatibility with EP matrix (Fig. 4b), but also endows their with multiple flame retardant effects. As expected, the incorporation of RGO@Ni(OH)$_2$ hybrid into EP/*h*BN can further decrease the PHRR, THR and TSP to 756.8 kW/m^2, 54.0 MJ/m^2 and 35.6 m^2, respectively, corresponding to a reduction of 33.5%, 33.8% and 43.0% comparing to neat EP, and a reduction of 10.5%, 21.4% and 23.9% comparing to EP/*h*BN. More importantly, the TTI value exhibits a dramatic improvement in EP/*h*BN/RGO@Ni(OH)$_2$ (103 s) comparing to neat EP (67 s) and EP/*h*BN (45 s), which is ascribed to the drastic increase of melt viscosity according to our previous reports [37,47]. Combing with the remarkable improvement in LOI value (29.2 vol%) and burning rate (V-1, self-quenching and no dripping) of EP/*h*BN/RGO@Ni(OH)$_2$, it can be concluded that an significant synergistic enhancement in flame retardancy and smoke suppression between RGO@Ni(OH)$_2$ hybrid and *h*BN occurs in their EP-based composites, which would be discussed in the following section. In addition, the fire growth rate index (FIGRA) calculated from the ratio of PHRR and time to PHRR [58], also reveals a considerable reduction of flammability in EP/*h*BN/RGO@Ni(OH)$_2$ by comparing with EP and EP/*h*BN (Table 1), which suggests that the flashover time of fire would be delayed in a real fire hazard.

To reveal the possible synergistic flame retardant mechanism between *h*BN sheets and RGO@Ni(OH)$_2$ hybrid for their EP-based composites, the morphology and components of chars after CC test were analyzed in detail. The mass loss curves during CC tests (Fig. 7d) reveals that neat EP loss more than its initial a mass of 90% after the combustion. Adding *h*BN sheets into EP matrix can signally improve the char yield with an intact but pulverulent white char layer (Fig. S7). A porous structure morphology (Fig. 8a), which is regarded as the transmission channels for the volatile products, oxygen and heat [59], is observed in the inner of char. Its high-magnification SEM image (Fig. 8b) and EDX spectrum (Fig. 8c) reveal that the char is composed of the stacking *h*BN sheets and few amorphous carbon. Based on these results, the relatively low flame retardancy of EP/*h*BN is thus attributed to the loose and porous char structure induced by the lack of organic sticking substance. For EP/*h*BN/RGO, introducing RGO can further improve the char yield. Although the integrity of char layer are somewhat broken, its block-like structure suggests that the quality of char layer is improved somewhat by RGO (Fig. S7). The char's inner morphology (Fig. 8d) also reveals the porous structure but with a decreasing pore size comparing to that of EP/*h*BN. Some organic carbide as binders can be confirmed by the high-resolution morphology and component analyses of char (Fig. 8e and f). However, the relatively low amount of organic carbide does not yet improve the char's strength effectively, so as to collapse as clumps. By contrast, EP/*h*BN/RGO@Ni(OH)$_2$ exhibits a more excellent char layer after combustion, including the char's yield and integrality (Fig. S7). The inner porous structure of its char layer shows a further decreasing pore size and compacted skeletons with lots of organic carbide as binder (Fig. 8g–i), which suggests the more effective barrier effect during its burning, further resulting in the obvious improvement of flame retardancy of EP/*h*BN/RGO@Ni(OH)$_2$. Moreover, some nanoparticles with a size of 100–200 nm are found in its high-resolution SEM image (inset in Fig. 8h), which are confirmed to be NiO/Ni nanoparticles by the EDX spectrum (Fig. 8i). The formation of these nanoparticles during burning proves the aforementioned multiple flame retardant effects of RGO@Ni(OH)$_2$.

The synergistic flame retardant mechanism between *h*BN sheets and RGO@Ni(OH)$_2$ hybrid in EP matrix is shown in Scheme 2, according to the above-mentioned analysis. Firstly, the multiple flame retardant effects of RGO@Ni(OH)$_2$ hybrid including endothermic effect (thermal decomposition of Ni(OH)$_2$) [60], catalytic carbonization and free radical adsorption ability (NiO/Ni nanoparticles products) [61], as well as the barrier effect of RGO [62], can reduce the burning temperature, dilute the concentration of oxygen and flammable gases, and increase the yield of organic chars during combustion of EP/*h*BN/RGO@Ni(OH)$_2$. Secondly, *h*BN sheets, combining with the forming organic chars act as "tortuous path" effect to prevent the transfer of heat, oxygen and volatile products [56]. Finally, the improving dispersion and interfacial interaction of RGO and *h*BN in matrix by coating Ni(OH)$_2$ nanoribbon are able to enhance the above-mentioned flame retardant effects. Therefore, the main condensed phase strategy, *i.e.,* the compact and robust protective char layer formed by catalytic carbonization of RGO@Ni(OH)$_2$ hybrid and the template effect of *h*BN sheets, as well as the assistant gas phase strategy including dilution effect and free radical adsorption, results in the obvious improvement in flame retardancy of EP/*h*BN/RGO@Ni(OH)$_2$ composite.

4. Conclusions

In summary, multiple synergistic effects of *h*BN and few graphene-hybrid were employed to improve the TC and flame retardancy of PTCs, simultaneously. Firstly, Ni(OH)$_2$ nanoribbon was synthesized by a simple, high-efficiency and eco-friendly hydrothermal process, which was used to flame-retardant functionalize RGO for the first time through electrostatic-assembly by a further hydrothermal process. The resulted flame retardant functionalized graphene (RGO@Ni(OH)$_2$ hybrid) was then incorporated into EP/*h*BN composites toward address the problems of low TC and high fire hazard of PTCs. Because of the strong hydrogen-bond interaction between Ni(OH)$_2$ and polymer matrix, the RGO@Ni(OH)$_2$ hybrid showed a good dispersion and interfacial adhesion in EP matrix, which further suppress the stacking aggregation behavior of *h*BN sheets at high filler loading. As a consequence, combining to the bridging effect of graphene between the adjacent *h*BN sheets, the TC of EP/*h*BN/RGO@Ni(OH)$_2$ composites presented a considerable enhancement when comparing to EP/*h*BN and neat EP after 20 wt% *h*BN loading. Moreover, the ternary composite with only 2 wt% RGO@Ni(OH)$_2$ also exhibited a high fire resistance with a high LOI value of 29.2% and V-1 burning rate. The significant

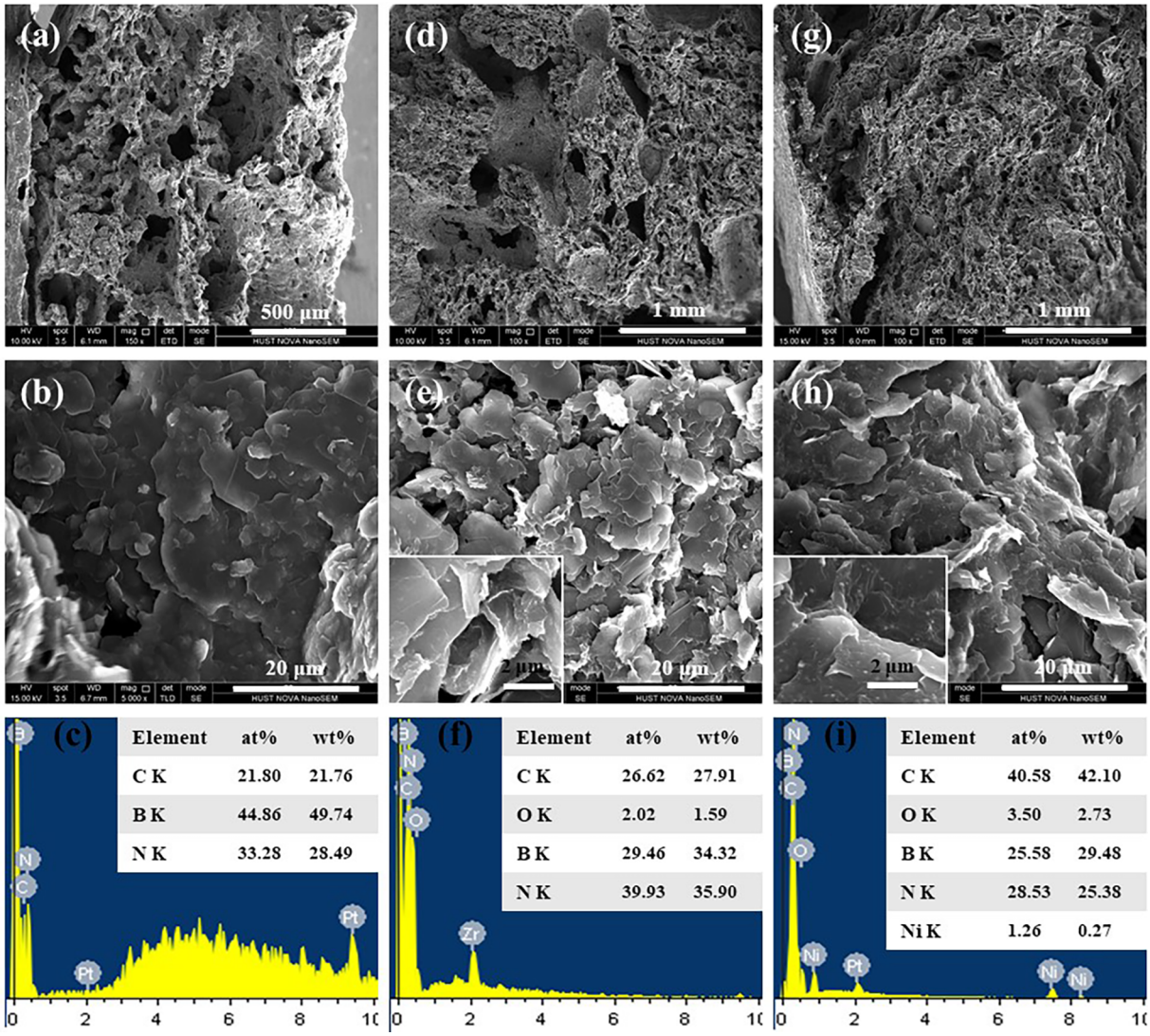

Fig. 8. SEM images of the residues after cone test with different magnification and EDX spectra of (a–c) EP/*h*BN, (d–f) EP/*h*BN/RGO and (g–i) EP/*h*BN/RGO@Ni$(OH)_2$ composites.

flame retardant parameters of HRR, THR and TSP showed a drastic reduction of 33.5%, 33.8% and 43.0% comparing to neat EP. The chars analysis revealed that the multiple flame retardant effects of RGO@Ni$(OH)_2$ hybrid, including dilution/cooling effect, free radical adsorption, catalytic carbonization and barrier effect, as well as the "tortuous path" effect of *h*BN sheets contributed to the improvement of flame retardancy.

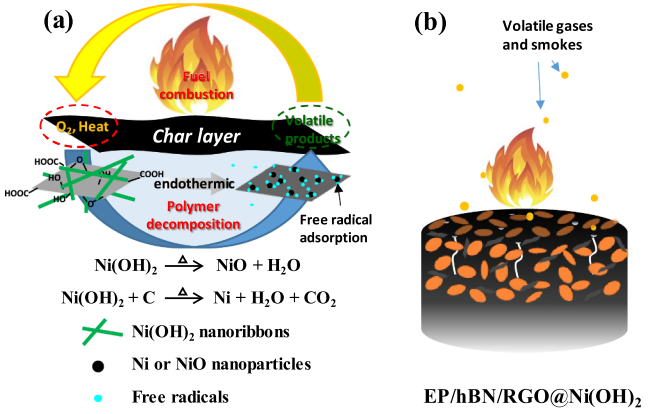

Scheme 2. Schematic illustration of (a) the flame-retardation effects of RGO@Ni$(OH)_2$ in EP matrix, and the flame retardation mechanism of (b) EP/*h*BN/RGO@Ni$(OH)_2$.

Acknowledgements

The authors gratefully acknowledge the financial support for this work by the National Science Foundation of China (Grant Nos. 51273073 and 51673076), the China Postdoctoral Science Foundation (Grant No. 2018M642781) and the analytical and testing assistance from the Analysis and Testing Center of HUST.

Appendix A. Supplementary data

Supplementary data to this article can be found online at https://doi.org/10.1016/j.cej.2019.122402.

References

[1] S.V. Garimella, A.S. Fleischer, J.Y. Murthy, A. Keshavarzi, R. Prasher, C. Patel, S.H. Bhavnani, R. Venkatasubramanian, R. Mahajan, Y. Joshi, B. Sammakia, B.A. Myers, L. Chorosinski, M. Baelmans, P. Sathyamurthy, P.E. Raad, Thermal challenges in next-generation electronic systems, IEEE Trans. Compon. Packag. Technol. 31 (2008) 801–815.

[2] A. Bar-Cohen, K. Matin, S. Narumanchi, Nanothermal interface materials: technology review and recent results, J. Electron. Packag. 137 (2015) 040803–040817.
[3] Z. Han, A. Fina, Thermal conductivity of carbon nanotubes and their polymer nanocomposites: a review, Prog. Polym. Sci. 36 (2011) 914–944.
[4] X. Xu, J. Chen, J. Zhou, B. Li, Thermal conductivity of polymers and their nanocomposites, Adv. Mater. 30 (2018) 1705544.
[5] F. Sarvar, D.C. Whalley, P.P. Conway. Thermal interface materials – a review of the state of the art. Electron. Syst. Technol. Conf. 2006. 1st ed., vol. 22006. pp. 1292–1302.
[6] Y. Feng, J. Hu, Y. Xue, C. He, X. Zhou, X. Xie, Y. Ye, Y.-W. Mai, Simultaneous improvement in the flame resistance and thermal conductivity of epoxy/Al_2O_3 composites by incorporating polymeric flame retardant-functionalized graphene, J. Mater. Chem. A 5 (2017) 13544–13556.
[7] N. Burger, A. Laachachi, M. Ferriol, M. Lutz, V. Toniazzo, D. Ruch, Review of thermal conductivity in composites: mechanisms, parameters and theory, Prog. Polym. Sci. 61 (2016) 1–28.
[8] Y. Feng, B. Wang, X. Li, Y. Ye, J. Ma, C. Liu, X. Zhou, X. Xie, Enhancing thermal oxidation and fire resistance for reduced graphene oxide by phosphorus and nitrogen co-doping: mechanism and kinetic analysis, Carbon 146 (2019) 650–659.
[9] H. Zhang, Ultrathin two-dimensional nanomaterials, ACS Nano 9 (2015) 9451–9469.
[10] C. Tan, X. Cao, X.-J. Wu, Q. He, J. Yang, X. Zhang, J. Chen, W. Zhao, S. Han, G.-H. Nam, M. Sindoro, H. Zhang, Recent advances in ultrathin two-dimensional nanomaterials, Chem. Rev. 117 (2017) 6225–6331.
[11] D. Golberg, Y. Bando, Y. Huang, T. Terao, M. Mitome, C. Tang, C. Zhi, Boron nitride nanotubes and nanosheets, ACS Nano 4 (2010) 2979–2993.
[12] Q. Weng, X. Wang, X. Wang, Y. Bando, D. Golberg, Functionalized hexagonal boron nitride nanomaterials: emerging properties and applications, Chem. Soc. Rev. 45 (2016) 3989–4012.
[13] X. Li, Y. Feng, C. Chen, Y. Ye, H. Zeng, H. Qu, J. Liu, X. Zhou, S. Long, X. Xie, Highly thermally conductive flame retardant epoxy nanocomposites with multifunctional ionic liquid flame retardant-functionalized boron nitride nanosheets, J. Mater. Chem. A 6 (2018) 20500–20512.
[14] C. Chen, Y. Xue, Z. Li, Y. Wen, X. Li, F. Wu, X. Li, D. Shi, Z. Xue, X. Xie, Construction of 3D boron nitride nanosheets/silver networks in epoxy-based composites with high thermal conductivity via in-situ sintering of silver nanoparticles, Chem. Eng. J. 369 (2019) 1150–1160.
[15] W. Jin, L. Yuan, G. Liang, A. Gu, Multifunctional cyclotriphosphazene/hexagonal boron bitride hybrids and their flame retarding bismaleimide resins with high thermal conductivity and thermal stability, ACS Appl. Mater. Interfaces 6 (2014) 14931–14944.
[16] S. Chen, R. Xu, J. Liu, X. Zou, L. Qiu, F. Kang, B. Liu, H.-M. Cheng, Simultaneous production and functionalization of boron nitride nanosheets by sugar-assisted mechanochemical exfoliation, Adv. Mater. 31 (2019) 1804810.
[17] W. Lei, V.N. Mochalin, D. Liu, S. Qin, Y. Gogotsi, Y. Chen, Boron nitride colloidal solutions, ultralight aerogels and freestanding membranes through one-step exfoliation and functionalization, Nat. Commun. 6 (2015) 8849.
[18] Z. Su, H. Wang, X. Ye, K. Tian, W. Huang, J. He, Y. Guo, X. Tian, Synergistic enhancement of anisotropic thermal transport flexible polymer composites filled with multi-layer graphene (mG) and mussel-inspiring modified hexagonal boron nitride (h-BN), Compos. A Appl. Sci. Manuf. 111 (2018) 12–22.
[19] Y.-J. Xiao, W.-Y. Wang, T. Lin, X.-J. Chen, Y.-T. Zhang, J.-H. Yang, Y. Wang, Z.-W. Zhou, Largely enhanced thermal conductivity and high dielectric constant of poly(vinylidene fluoride)/boron nitride composites achieved by adding a few carbon nanotubes, J. Phys. Chem. C 120 (2016) 6344–6355.
[20] T. Zhou, X. Wang, X. Liu, D. Xiong, Improved thermal conductivity of epoxy composites using a hybrid multi-walled carbon nanotube/micro-SiC filler, Carbon 48 (2010) 1171–1176.
[21] S. Choi, H. Im, J. Kim, The thermal conductivity of embedded nano-aluminum nitride-doped multi-walled carbon nanotubes in epoxy composites containing micro-aluminum nitride particles, Nanotechnology 23 (2012) 065303.
[22] W.-B. Zhang, Z.-X. Zhang, J.-H. Yang, T. Huang, N. Zhang, X.-T. Zheng, Y. Wang, Z.-W. Zhou, Largely enhanced thermal conductivity of poly(vinylidene fluoride)/carbon nanotube composites achieved by adding graphene oxide, Carbon 90 (2015) 242–254.
[23] A. Yu, P. Ramesh, X. Sun, E. Bekyarova, M.E. Itkis, R.C. Haddon, Enhanced thermal conductivity in a hybrid graphite nanoplatelet-carbon nanotube filler for epoxy composites, Adv. Mater. 20 (2008) 4740–4744.
[24] D. Suh, C.M. Moon, D. Kim, S. Baik, Ultrahigh thermal conductivity of interface materials by silver-functionalized carbon nanotube phonon conduits, Adv. Mater. 28 (33) (2016) 7220–7227.
[25] N. Song, H. Pan, X. Hou, S. Cui, L. Shi, P. Ding, Enhancement of thermal conductivity in polyamide-6/graphene composites via a “bridge effect” of silicon carbide whiskers, RSC Adv. 7 (73) (2017) 46306–46312.
[26] X. Wang, E.N. Kalali, J.-T. Wan, D.-Y. Wang, Carbon-family materials for flame retardant polymeric materials, Prog. Polym. Sci. 69 (2017) 22–46.
[27] B. Sang, Z.-W. Li, X.-H. Li, L.-G. Yu, Z.-J. Zhang, Graphene-based flame retardants: a review, J. Mater. Sci. 51 (2016) 8271–8295.
[28] B. Yuan, Y. Hu, X. Chen, Y. Shi, Y. Niu, Y. Zhang, S. He, H. Dai, Dual modification of graphene by polymeric flame retardant and $Ni(OH)_2$ nanosheets for improving flame retardancy of polypropylene, Compos. A Appl. Sci. Manuf. 100 (2017) 106–117.
[29] Y. Feng, C. He, Y. Wen, Y. Ye, X. Zhou, X. Xie, Y.-W. Mai, Improving thermal and flame retardant properties of epoxy resin by functionalized graphene containing phosphorous, nitrogen and silicon elements, Compos. A Appl. Sci. Manuf. 103 (2017) 74–83.
[30] X. Wang, W. Xing, X. Feng, B. Yu, H. Lu, L. Song, Y. Hu, The effect of metal oxide decorated graphene hybrids on the improved thermal stability and the reduced smoke toxicity in epoxy resins, Chem. Eng. J. 250 (2014) 214–221.
[31] J. Han, Y. Dou, D. Yan, J. Ma, M. Wei, D.G. Evans, X. Duan, Biomimetic design and assembly of organic–inorganic composite films with simultaneously enhanced strength and toughness, Chem. Commun. 47 (2011) 5274–5276.
[32] Y. Hai, S. Jiang, X. Qian, S. Zhang, P. Sun, B. Xie, N. Hong, Ultrathin Beta-Nickel hydroxide nanosheets grown along multi-walled carbon nanotubes: a novel nanohybrid for enhancing flame retardancy and smoke toxicity suppression of unsaturated polyester resin, J. Colloid Interface Sci. 509 (2018) 285–297.
[33] L. Dong, C. Hu, X. Huang, N. Chen, L. Qu, One-pot synthesis of nitrogen and phosphorus co-doped graphene and its use as high-performance electrocatalyst for oxygen reduction reaction, Chem. Asian J. 10 (2015) 2609–2614.
[34] Q. Kong, T. Wu, Y. Tang, L. Xiong, H. Liu, J. Zhang, R. Guo, F. Zhang, Improving thermal and flame retardant properties of epoxy resin with organic NiFe-layered double hydroxide-carbon nanotubes hybrids, Chin. J. Chem. 35 (2017) 1875–1880.
[35] N. Hong, J. Zhan, X. Wang, A.A. Stec, T. Richard Hull, H. Ge, W. Xing, L. Song, Y. Hu, Enhanced mechanical, thermal and flame retardant properties by combining graphene nanosheets and metal hydroxide nanorods for Acrylonitrile–Butadiene–Styrene copolymer composite, Compos. A Appl. Sci. Manuf. 64 (2014) 203–210.
[36] N. Hong, L. Song, B. Wang, A.A. Stec, T.R. Hull, J. Zhan, Y. Hu, Co-precipitation synthesis of reduced graphene oxide/NiAl-layered double hydroxide hybrid and its application in flame retarding poly(methyl methacrylate), Mater. Res. Bull. 49 (2014) 657–664.
[37] Y. Feng, X. Li, X. Zhao, Y. Ye, X. Zhou, H. Liu, C. Liu, X. Xie, Synergetic improvement in thermal conductivity and flame retardancy of epoxy/silver nanowires composites by incorporating “branch-like” flame-retardant functionalized graphene, ACS Appl. Mater. Interfaces 10 (25) (2018) 21628–21641.
[38] C. He, S. Qiu, H. Peng, Q. Zhang, X. Han, Y. Yang, D. Shi, X. Xie, Combination of 1D Ni(OH)2 nanobelts and 2D graphene sheets to fabricate 3D composite hydrogel electrodes with ultrahigh capacitance and superior rate capability, Compos. Sci. Technol. 167 (2018) 155–163.
[39] R.N. Rothon, P.R. Hornsby, Flame retardant effects of magnesium hydroxide, Polym. Degrad. Stabil. 54 (2) (1996) 383–385.
[40] C.L. Cronan, F.J. Micale, M. Topić, H. Leidheiser, A.C. Zettlemoyer, S. Popovic, Surface properties of $Ni(OH)_2$ and NiO. II. Mechanism for the thermal decomposition of $Ni(OH)_2$ and other metal hydroxides, J. Colloid Interface Sci. 55 (1976) 546–557.
[41] S.-I. Kim, J.-S. Lee, H.-J. Ahn, H.-K. Song, J.-H. Jang, Facile Route to an efficient NiO supercapacitor with a three-dimensional nanonetwork morphology, ACS Appl. Mater. Interfaces 5 (5) (2013) 1596–1603.
[42] P. Kumar, F. Shahzad, S. Yu, S.M. Hong, Y.H. Kim, M.K. Chong, Large-area reduced graphene oxide thin film with excellent thermal conductivity and electromagnetic interference shielding effectiveness, Carbon 94 (2015) 494–500.
[43] Z. Li, J. Han, L. Fan, M. Wang, S. Tao, R. Guo, The anion exchange strategy towards mesoporous α-$Ni(OH)_2$ nanowires with multinanocavities for high-performance supercapacitors, Chem. Commun. 51 (2015) 3053–3056.
[44] L. Liang, G. Han, Y. Li, B. Zhao, B. Zhou, Y. Feng, J. Ma, Y. Wang, R. Zhang, C. Liu, A promising $Ti_3C_2T_x$ MXene/Ni chain hybrid with excellent electromagnetic wave absorption and shielding capacity, ACS Appl. Mater. Interfaces (2019), https://doi.org/10.1021/acsami.9b07294.
[45] F. Tuinstra, J.L. Koenig, Raman spectrum of graphite, J. Chem. Phys. 53 (1970) 1126–1130.
[46] J. Yan, Z. Fan, W. Sun, G. Ning, T. Wei, Q. Zhang, R. Zhang, L. Zhi, F. Wei, Advanced asymmetric supercapacitors based on $Ni(OH)_2$/graphene and porous graphene electrodes with high energy density, Adv. Funct. Mater. 22 (2012) 2632–2641.
[47] Y. Feng, C. He, Y. Wen, Y. Ye, X. Zhou, X. Xie, Y.-W. Mai, Superior flame retardancy and smoke suppression of epoxy-based composites with phosphorus/nitrogen co-doped graphene, J. Hazard. Mater. 346 (2018) 140–151.
[48] Z. Tang, H. Kang, Z. Shen, B. Guo, L. Zhang, D. Jia, Grafting of polyester onto graphene for electrically and thermally conductive composites, Macromolecules 45 (8) (2012) 3444–3451.
[49] Y.J. Mai, J.P. Tu, C.D. Gu, X.L. Wang, Graphene anchored with nickel nanoparticles as a high-performance anode material for lithium ion batteries, J. Power Sources 209 (2012) 1–6.
[50] K. Kim, J. Kim, Exfoliated boron nitride nanosheet/MWCNT hybrid composite for thermal conductive material via epoxy wetting, Compos. B Eng. 140 (2018) 9–15.
[51] C. Yuan, B. Duan, L. Li, B. Xie, M. Huang, X. Luo, Thermal Conductivity of polymer-based composites with magnetic aligned hexagonal boron nitride platelets, ACS Appl. Mater. Interfaces 7 (2015) 13000–13006.
[52] H. Ribeiro, J.P.C. Trigueiro, P.S. Owuor, L.D. Machado, C.F. Woellner, J.J. Pedrotti, Y.M. Jaques, S. Kosolwattana, A. Chipara, W.M. Silva, C.J.R. Silva, D.S. Galvão, N. Chopra, I.N. Odeh, C.S. Tiwary, G.G. Silva, P.M. Ajayan, Hybrid 2D nanostructures for mechanical reinforcement and thermal conductivity enhancement in polymer composites, Compos. Sci. Technol. 159 (2018) 103–110.
[53] J.C.M. Garnett, Colours in metal glasses and in metallic films, Proc. R. Soc. London 73 (1904) 443–445.
[54] C.-W. Nan, R. Birringer, D.R. Clarke, H. Gleiter, Effective thermal conductivity of particulate composites with interfacial thermal resistance, J. Appl. Phys. 81 (1997) 6692–6699.
[55] S.-Y. Yang, W.-N. Lin, Y.-L. Huang, H.-W. Tien, J.-Y. Wang, C.-C.M. Ma, S.-M. Li, Y.-S. Wang, Synergetic effects of graphene platelets and carbon nanotubes on the mechanical and thermal properties of epoxy composites, Carbon 49 (2011) 793–803.

[56] B. Yu, W. Xing, W. Guo, S. Qiu, X. Wang, S. Lo, Y. Hu, Thermal exfoliation of hexagonal boron nitride for effective enhancements on thermal stability, flame retardancy and smoke suppression of epoxy resin nanocomposites via sol-gel process, J. Mater. Chem. A 4 (2016) 7330–7340.
[57] E.N. Kalali, X. Wang, D.-Y. Wang, Multifunctional intercalation in layered double hydroxide: toward multifunctional nanohybrids for epoxy resin, J. Mater. Chem. A 4 (2016) 2147–2157.
[58] B. Yu, Y. Shi, B. Yuan, S. Qiu, W. Xing, W. Hu, L. Song, S. Lo, Y. Hu, Enhanced thermal and flame retardant properties of flame-retardant-wrapped graphene/epoxy resin nanocomposites, J. Mater. Chem. A 3 (2015) 8034–8044.
[59] T. Kashiwagi, F. Du, J.F. Douglas, K.I. Winey, R.H. Harris, J.R. Shields, Nanoparticle networks reduce the flammability of polymer nanocomposites, Nat. Mater. 4 (2005) 928–933.
[60] H. Cao, H. Zheng, J. Yin, Y. Lu, S. Wu, X. Wu, B. Li, Mg(OH)2 Complex nanostructures with superhydrophobicity and flame retardant effects, J. Phys. Chem. C 114 (2010) 17362–17368.
[61] N. Hong, L. Song, T.R. Hull, A.A. Stec, B. Wang, Y. Pan, Y. Hu, Facile preparation of graphene supported Co_3O_4 and NiO for reducing fire hazards of polyamide 6 composites, Mater. Chem. Phys. 142 (2013) 531–538.
[62] B. Dittrich, K.-A. Wartig, D. Hofmann, R. Mülhaupt, B. Schartel, Flame retardancy through carbon nanomaterials: carbon black, multiwall nanotubes, expanded graphite, multi-layer graphene and graphene in polypropylene, Polym. Degrad. Stabil. 98 (2013) 1495–1505.